Volume 1 | Number 1 | Jan 2013 | Pages 1–100

ROYAL SOCIETY
OF CHEMISTRY

ROYAL SOCIETY
OF CHEMISTRY

www.rsc.org/catalysis

Catalysis
Science & Technology

ARTICLE

New multicomponent catalysts for the selective aerobic oxidative condensation of benzylamine to N-benzylidenbenzilimine

C.M. Opriş,[a] O.D. Pavel,[a] A. Moragues,[b] J. El Haskourib,[c] D. Beltrán,[b] P. Amorós,[b,*] M.D. Marcos,[d] L.E. Stoflea,[e] V.I. Parvulescu[a,*]

Aerobic oxidative condensation of benzylamine to N-benzylidenbenzilamine was carried out on new gold-based catalysts using as supports bimodal UVM-7-like mesoporous silica, containing Ni and Ce (or Sn) as oxide nanodomains partially embedded inside the mesoporous UVM-7 silica walls. These nano-domains acted as effective and stable inorganic anchors favoring the nucleation, growth and stability of supported gold particles. Following the Atrane method (a "one pot" strategy able to harmonize the hydrolytic reactivity of different heteroelements through the use of complexes containing triethanolamine derived ligands (atranes) as precursors the stability of the oxide nanodomains during oxidation and thermal treatments was ensured. The catalysts were prepared in a two-step synthesis in which gold was incorporated through impregnation of previously synthesized bimodal porous silicas containing different heteroelements trapped by the silica mesostructure. The versatility of the preparative approach allowed high surface and accessibility of the mesoporous silica and also an easy and homogeneous inclusion of heteroelements in one pot. Aerobic oxidative condensation of benzylamine on these catalysts occurred selectively only with the formation of N-benzylidenbenzylamine. While the selectivity was total, the productivities ($mol_{product}$ g_{cat}^{-1} h^{-1}) varied in a large range as a function of the catalyst composition (chemical composition and atomic ratios of the constitutive support elements). The catalytic behavior was merely controlled by the size of the gold particles, but the support is also exerting an influence. The best results were obtained on the mesoporous Au/Ce_{60}-Ni_{10}-UVM-7 catalyst having a 0.97(wt.%) gold content (in the form of nanoparticles of ca. 4 nm) and preserving a relatively high surface (566 m^2/g) and pore volume (0.91 cm^3/g). The comparison with the individual or bicomponent catalysts led to the conclusion of a cooperative interaction between the catalysts components. However, gold itself exhibits a higher activity than the promoters or co-catalysts (*ie* phases containing Ni or/and Ce).

1. Introduction

Catalytic selective oxidation of benzylamine to corresponding imine is an important reaction in organic chemistry since the product of reaction is a valuable intermediate in organic synthesis.[1] Imines, due to their reactivity, have multiple applications[2, 3] as building blocks for the manufacture of fine chemicals, pharmaceutics,[4] agrochemicals, dyes, polymers,[5] lipoxygenase inhibitors, anti-inflammatory and anti-cancer agents.[6] They can undergo a large variety of transformations including hydrogenations, cycloadditions and nucleophilic additions.[7]
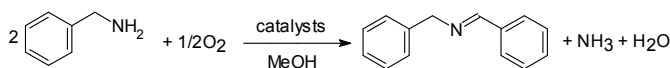
Traditionally, aerobic oxidative condensation of benzylamines to imines is performed using stoichiometric amounts of oxidants[8, 9] or by condensation of carbonyl compound with amines in the presence of a Lewis acid catalyst: $TiCl_4$, Al_2O_3, $MgSO_4$, K-10.[6] Due to recent considerations of environmental issues, the use of stoichiometric reagent is undesirable.[9] In addition, some disadvantages such as complex procedures, long reaction time, high temperature and use of aromatic solvents [10] led to the development of catalytic systems which use as oxidants organic and inorganic peroxides.[11] A green alternative is the use of oxygen as final oxidant. Unfortunately, the reactivity of molecular oxygen is difficult to be controlled, and as a consequence, the selectivity of the reaction is rather low.[4] Aerobic oxidative condensation of benzylamine leads to a Schiff base through the oxidative dehydrogenation of primary amine and, consequently, to the condensation with a second molecule of unreacted amine.[12] This reaction takes place in presence of various catalysts, such as: Au/CeO_2,[13] Au/TiO_2, Au/C, Au/Al_2O_3,[14] Pd/TiO_2, Pt/TiO_2,[7, 15] CuCl, $CuCl_2$,[16] gold powder,[17] rhodium complexes,[6] Au, Au-Pd and Pd supported on porous steel fiber matrices,[8] doped polyaniline emeraldine salt.[18] Results for this reaction conducted under ultrasound irradiation in the presence of solid supported catalysts (clay, silica or resin)[19] or under photochemical irradiation with the use of molecular oxygen in the presence of acridinium salts,[20] mesoporous graphite carbon nitride,[21] or TiO_2 as

photocatalysts were reported as well. In addition, working under microwave irradiation allows the free-solvent synthesis of imines, but this method is limited to few compounds. Moreover, it uses magnesium perchlorate as catalyst, which is known for its potential explosive character.[10] Recent advances on the aerobic oxidation of amines have been discussed in several review papers including results achieved by using gold-based catalysts.[22, 23] The relevance of these nano-gold catalysts in fine chemical synthesis has been also reviewed.[24]

Supported gold nanoparticles were reported to exhibit high activity in the selective aerobic oxidative condensation of benzylamines to N-benzylidenbenzilamine. Obviously, using gold as catalyst, in addition to the particle size (typically less than 5 nm large, the gold catalyst efficiency increased exponentially as the average gold particle size decreased),[7, 14, 15, 17, 25-28] the nature of support is very important.[7, 23, 29-31] Indeed, a series of supports such as reducible Co_3O_4, ZnO, TiO_2, Fe_2O_3, and nanocrystalline Ce_2O_3 reducible oxides but also carbons have been indicated as being adequate for preparing highly active gold supported catalysts, while others such as non-reducible SiO_2 and Al_2O_3 oxides were reported as less efficient.[26] In a recent paper Wachs and Routray indicated NiO as exhibiting surface active sites and reactivity in oxidation reactions close to ceria.[32] In another recent report, the peculiar influence of a NiO support was studied by preparing supported gold catalysts where Au nanoparticles showed high activity for the selective oxidation of glycerol and ethane-1,2-diol. A detailed characterization of the resulting Au catalysts revealed a preferential deposition of the metal nanoparticles on the NiO phase.[33] On the other side Au/Ni_2O_3 was indicated as an efficient catalyst for low-temperature gas-phase oxidation of alcohols.[34] Au supported on tin oxides also showed interesting oxidation properties. Gold-supported tin dioxide nanocatalysts are active for low-temperature CO oxidation,[35] while gold nanoparticle doped hollow SnO_2 super-symmetric nanostructures demonstrated improved photocatalytic properties.[36]

Taking into account the state of the art (ie, the role of size of gold nano-particles in this reaction and of reducible nano-oxide supports and of NiO in selective oxidations) herein we propose new materials for aerobic oxidative condensation of benzylamine to N-benzylidenbenzilamine (Scheme 1) able to achieve high conversions and selectivities in a very short range of time. The new gold-based catalysts considered a more complex support. In this work we prepared Ni, Ce (or Sn) as oxide nanodomains partially embedded inside the mesoporous UVM-7 silica walls as effective and stable inorganic anchors favoring the nucleation, growth and stability of supported gold particles. Following the Atrane method (a "one pot" strategy able to harmonize the hydrolytic reactivity of different inorganic precursors)[37] the stability of the oxide nanodomains during oxidation and thermal treatments was ensured. After the deposition of gold using the deposition/precipitation procedure nano-gold particles in direct interaction with the Ni, Ce (or Sn) oxide nanodomains were generated. The versatility of the preparative approach used allows us to exploit both the high surface and accessibility of the mesoporous silica and also an easy and homogeneous inclusion of heteroelements in one pot.

Scheme 1. Aerobic oxidative condensation of benzylamine to N-benzylidenbenzilimine.

2. Experimental details

2.1. Catalysts preparation

All the synthesis reagents are analytically pure, and were used as received from Aldrich: tetraethyl orthosilicate [TEOS], nickel nitrate, cerium and tin chlorides, triethanolamine [hereinafter TEA], cetyltrimethylammonium bromide [CTABr] and $HAuCl_4\cdot3H_2O$.

All the catalysts were prepared in a two-step synthesis in which gold was incorporated through impregnation of previously synthesized bimodal porous silicas containing different heteroelements. In order to analyze the effect of the different species included inside the pore walls, we have prepared materials containing (in addition to Si) only Ni (Ni_x-UVM-7 materials), Ni and Ce (Ce_y-Ni_x-UVM-7) and Ni and Sn (Sn_y-Ni_x-UVM-7). The heteroelement incorporation inside the silica walls was carried out using the Atrane method.[37] This one-pot method is based on the use of complexes (detected through mass-spectral analysis) that include TEA-related ligand species (*i.e.*, "atranes" of Si, Ni, Ce and Sn in the present case) as hydrolytic inorganic precursors and surfactant micelles as templating agents able to generate mesopores after its evolution. In all cases the use of TEA plays a double role: as ligand to form the atranes and as buffer agent to stabilize the pH around 9-10, favoring the isolation of a bimodal nanoparticulated rich silica support.[38, 39] A typical synthesis leading to support Ce_{10}-Ni_{10}-UVM-7 (see Table 1) can be described as follows: (1) a mixture of TEOS (11 mL, 0.045 mol), $CeCl_3$ (1.84 gr, $4.94.10^{-3}$ mol) and $Ni(NO_3)\cdot5H_2O$ (1.43 gr, $4.94.10^{-3}$ mol) was slowly added to liquid TEA (23 mL, 0.17 mol), and heated at 150 °C for 10 min to give a mixture of atrane complexes. After cooling of the previous solution to 90 °C, CTABr (4.77 g, 0.014 mol) was added and dissolved. This last solution containing the atrane complexes and the template was cooled to 60 °C and mixed with water (80 mL, 4.44 mol). After a few seconds, a white powder appeared and it was allowed to age at room temperature for 4 h. The final mesostructured powder was filtered off, washed with water and ethanol, and air-dried. Finally, surfactant removal was accomplished through calcination at 550 °C (ramp heating: 1 degree/min) for 7 h. In all cases, the molar ratio of the reagents in the mother liquor was adjusted to 2 Si: *a* Ni: *b* Ce or Sn: 7 TEA: 0.52 CTABr: 180 H_2O (where *a* = 0.033, 0.066 and 0.2, and *b*= 0 for samples Ni_x-UVM-7; *a* = 0.2, and *b* = 0.033, 0.066 and 0.2 for samples denoted as $Ce(Sn)_yNi_{10}$-UVM-7). Samples are denoted as $Ce(Sn)_y$-Ni_x-UVM-7, where x and y are the Si/Ni and Si/Ce(Sn) nominal atomic ratios, respectively. Regardless of the nature and composition of the support, the gold incorporation was carried out by the same procedure.

Gold was incorporated through deposition-precipitation in aqueous $HAuCl_4\cdot3H_2O$ solutions.[40] The porous supports (1 g) were suspended in an aqueous solution (10 mL) of $HAuCl_4\cdot3H_2O$ (2%). The pH was adjusted to 8-9 with an aqueous NaOH solution and was then aged for 1 h under stirring at 75°C. In fact, at the working pH, $Au(OH)_4^-$ species are dominant.[41, 42] The low isoelectric point of the silica surface (*ca.* 2–3) hinders the interaction with anionic species. $Au(OH)_4^-$ complexes require a positively charged surface provided by NiO_x and CeO_2 anchoring nanodomains having *zpc* values in the 9.9-11.3 and 6.7-8.6 ranges, respectively. As occurs for the silica surface, no anchoring effects are expected for the SnO_2 domains taking into account its relatively low *zpc* value (4.5-5). Then, Au complexes will interact in a preferred way on the NiO_x nanodomains embedded inside the mesopore walls instead of on the silica surface and to a lesser extent on the CeO_2 particles. The resulting homogeneity and dispersion of gold particles will reflect the achieved for NiO_x anchors.

The solids were filtered and exhaustively washed with water to favor evolution of the adsorbed Cl⁻ species, which usually leads to catalysts poisoning. Finally, the solid was dried at 80ºC overnight and calcined at two different temperatures, 200 or 500ºC, for 1h in static air in order to favor the reduction of the Au-complexes and the formation of gold nanoparticles.

In this way, three families of gold catalysts were obtained: Au/Ni$_{10}$-UVM-7(T), Au/Ce$_x$-Ni$_{10}$-UVM-7(T) and Au/Sn$_x$-Ni$_{10}$-UVM-7(T) (T= 200, 500ºC). Table 1 summarizes the main synthesis variables and physical data. XPS analysis indicated no residual chlorine in the prepared catalysts.

For comparison, we synthesized two additional gold containing catalysts by impregnation of silica UVM-7 and commercial CeO$_2$ with a HAuCl$_4$·3H$_2$O solution following the strategy described in the bibliography.[43, 44] The loading of gold in these catalysts was of the same order with that in the multicomponent catalysts, ie 1.25 wt % and 1.19 wt%, respectively.

2.2. Catalysts characterization

Chemical analysis of the samples was carried out using electron probe microanalysis (EPMA, Philips SEM-515 instrument) and ICP-OES analysis (Agilent 710 Series ICP-OES). Powder X-ray diffraction patterns were recorded with a Seifert 3000TT θ–θ diffractometer using CuKα radiation. Patterns were collected in steps of 0.02º (2θ) over the angular ranges 1º–10º (2θ) or 10º–80º (2θ) for 25 s per step. The TEM and HRTEM microstructural characterizations were carried out using a JEOL JEM-1010 instrument operating at 100 kV and equipped with a CCD camera and a Tecnai G^{2}F20(FI) instrument, respectively. STEM-HAADF images were acquired on a JEOL-2100F microscope, and particle size distributions were determined from a total number of gold particles counted in the 300-400 range. The N$_2$ adsorption–desorption isotherms were recorded at –196 °C using a Micromeritics ASAP2020 automated instrument. Calcined samples were degassed for 15 h at 130 ºC and 10^{-6} Torr before analysis. Surface areas were estimated according to the BET model, and pore size dimensions were calculated using the BJH method. XPS spectra for both fresh and tested catalysts were recorded at room temperature using a SSX-100 spectrometer, Model 206 from Surface Science Instrument. The pressure in the analysis chamber during the analysis was 1.33 mPa. Monochromatized Al-K☐ radiation (h☐ = 1486.6 eV) generated by bombarding the Al anode with an electron gun operated with a beam current of 12 mA and acceleration voltage of 10 kV has been used. The spectrometer energy scale was calibrated using the Au 4f$_{7/2}$ peak centered at 83.98 eV. Charge correction was made with the C$_{1s}$ signal of adventitious carbon (C – C or C – H bonds) located at 284.8 eV. The atomic surface compositions were calculated using the sensitivity factors provided with the apparatus software, applied to the surface below the corresponding fitted XPS signals. An estimated error of ± 0.1 eV can be assumed for all measurements. The zeta potential of selected samples was measured at 25 °C using dynamic light scattering (Malvern Zetasizer Nano ZS instrument).

2.3. Catalytic tests

The catalytic activity tests were performed under batch conditions in the range of temperatures 75°C - 115°C. Experiments were performed in a 100 mL stainless steel autoclave provided with a magnetic stirrer, using an amount of 18.2 mmoles benzylamine (Sigma-Aldrich), and 0.12 moles methanol (Sigma-Aldrich), as solvent and a pressure of 5 bar

O$_2$ (Linde). *Note that in the presence of an ignition source, such as a spark or flame, there is a risk of explosion! Extreme precaution is necessary to avoid this danger.* The amount of the catalyst introduced in the reaction corresponded to 2x10^{-5} moles heteroelement (Ni, Ce, Sn). Diffusion constraints were checked with catalysts size between 170 and 400 ☐m and modifying the stirring rate in the range 0-1400 rpm. Particles size of 200 ☐m and a stirring rate of 1200 rpm eliminated any diffusional effects as it has been proved from the variation of the conversion. After 0.5-5 hours reaction time the autoclave was cooled and the catalyst separated by filtration. The liquid sample was analyzed by GC-MS using a Trace GC 2000 coupled with DSQ MS from Thermo Electron Corporation equipped with FID detector, a capillary column with DB5 stationary phase (30m length and 0.324 mm diameter), and highly pure N$_2$ (99.999%) as carrier gas. Ammonia resulted as by-product has been analyzed using a Dionex ICS3000 ion-chromatograph from Thermo equipped with a medium hydrophobic Dionex Ionpac CS18 analytical column using a 4 mM isocratic methanesulfonic acid eluent at a flow rate of 0.25 mL/min. The reproducibility of the results was carefully checked using the above analytic tools.

The performances of the catalysts were compared based on the conversion of the benzylamine and the selectivity to N-benzylidenbenzilamine. Since the reaction occurs with different rates on all the individual components the calculation of TOF for the multicomponent catalysts will change its meaning because the calculated value will correspond to a mean average value on all these components. Thus, to avoid any misinterpretations of the activity we calculated the productivity of the catalysts as mol$_{product}$ g$_{cat}$$^{-1}$ h^{-1} and the results were interpreted using this parameter consider as g$_{cat}$ the entire mass of the components exhibiting catalytic activity (Ni, Ce, Sn and Au) (see Table 2 and 3). However, for comparison TOF values were calculated for the catalysts containing gold, considering only the contribution of Au.

Blank experiments were performed in the same experimental set-up and the same range of temperatures (75°C - 115°C) using an amount of 18.2 mmoles benzylamine, 0.12 moles methanol, as solvent and a pressure of 5 bar O$_2$. In order to support the reaction mechanism additional experiments were carried out in the range of O$_2$ pressure of 1-5 bars, and experiments in which benzaldehyde was added to the reaction mixtures in the different stages of the reaction. In this respect benzylamine-to-benzaldehyde molar ratios between 5 and 1 were considered. Water has been also introduced in separate experiments in volumes of 1-20 μL using a chromatographic syringe.

To check the effect of water experiments with dried methanol from (Sigma-Aldrich, puriss.pa.), benzylamine (dried with 3 Å molecular sieves), and O$_2$ (passed on a 3 Å molecular sieves column) have been carried out too..

3. Results and discussion

3.1. Characterization

Tables 1-3 compile the analytic and textural characterization of the investigated samples. Regarding to the gold-free Ce(Sn)$_y$-Ni$_x$-UVM-7 mesoporous supports, summarized in Table 1 are the corresponding Si/Ni, Si/Ce and Si/Sn molar ratio values (averaged from data of about 50 different particles) of the resulting solids from EPMA and ICP-OES. All samples are chemically homogeneous at micrometric

level with a regular dispersion of Ni, Ce and Sn species (and silicon) throughout the inorganic walls at the spot size (*ca.* 1μm). EPMA shows that the reported $Ce(Sn)_y$-Ni_x-UVM-7 materials contain Si/Ce or Si/Sn molar ratios similar to those present in the mother solutions. This fact indicates that, in general, there is no preferential incorporation of Ce (or Sn) or Si into the porous solid walls. This behavior is related to the low solubility of Ce or Sn species under the working pH conditions,[42] and the consequently quick and easy formation of the respective oxides. On the contrary, the Ni content in the final solids is significantly lower than that present in the starting solutions. This fact could be tentatively attributed to the well-known affinity of nickel for nitrogen donors. It must be pointed out that, in aqueous solution TEA essentially behaves as a tertiary amine, and a certain nickel amount could be stabilized in solution in the form of Ni-TEA complexes. A similar tendency was observed in the case of Co-MCM-41 derivatives.[45]

All supports display low-angle XRD patterns with one strong peak and one broad signal of relatively low intensity (Fig. SI1), that can be associated to the (100) and the overlapped (110) and (200) reflections of a MCM-41-like hexagonal cell, respectively. These patterns are characteristic of hexagonal disordered UVM-7 mesoporous silicas. The observed regular and smooth shift of the (100) intense peak towards low 2θ(º) values as the heteroelement content increases suggests a certain growing process of the mesoporous wall sizes due to the incorporation (completely embedded or partially trapped) of the NiO_x, CeO_2 and SnO_2 nanodomains (as can be see below, the BJH pore sizes result practically unchanged). High-angle XRD patterns (Fig. SI2 and SI3) show appreciable differences dealing with the incorporation of the three heteroelements. Regardless the Ni, Ce or Sn content, no signals assigned to NiO_x oxides appears in the diffractograms. This is consistent with a good dispersion of Ni along the porous walls in the form of extremely low size nanodomains (<2 nm) as occurs for the incorporation of Co and Zn under similar conditions.[45, 46] On the contrary, even for the samples with lower Ce amount, we unambiguously observe several diffraction peaks due to the presence of crystalline CeO_2 particles. The intensity of these peaks increases while the *fwhm* decreases with the Ce content, as expected. This behavior is consistent with the high insolubility of ceria. Then, before blocking by the silica-surfactant mesostructure, the growing achieved by CeO_2 domains seems to be higher than those achieved for the NiO_x ones. An intermediate situation is observed for the tin incorporation. In this case, only for the Sn-rich supports SnO_2 diffraction peaks are appreciated. The low intensity and large *fwhm* of the SnO_2 peaks are indicative of very small crystallite sizes.

TEM images allow discarding segregation of non-porous oxides (NiO_x, CeO_2 or SnO_2) in the form of large particles (Fig.1). Images of medium magnification confirm the absence of non-porous particles that could be ascribed to Ni, Sn or Ce oxide. In fact, TEM images of the $Ce(Sn)_y$-Ni_x-UVM-7 supports (Fig. SI4 and 1) are very similar to those of pure UVM-7 silica and confirm that two pore systems are present: intraparticle mesopores (white spots in the TEM images; insets of Fig. SI4 and 1) and large inter-particle pores of textural-type. Changes in Ni content do not affect the UVM-7 morphology. Then, in the case of Ni_x-UVM-7 supports (free Ce or Sn samples) the TEM images are practically indistinguishable from those of UVM-7 silica. As the Ce or Sn content increased, although the UVM-7 morphology is preserved, we observe two

effects that principally affect the textural porosity: (a) a wider size distribution in the primary silica-based particles, and (b) a higher interparticle condensation (this favoring aggregation), when compared to pure UVM-7 or Ni_x-UVM-7 supports.

On the other hand, the above-mentioned absence of large-scale NiO_x, SnO_2 or CeO_2 segregation suggests that these particles must be basically present in the form of small nanodomains partially embedded inside the silica-based pore walls. TEM images display numerous small black spots with spherical or pseudo-spherical shapes with dimensions in the 2-7 nm range. Then, although a small segregation in the form of micrometric particles cannot be completely discarded (overcoat in the case of CeO_2), TEM micrographs are consistent with a homogeneous nano-dispersion of Ni, Sn and Ce oxidic domains forming together with the amorphous silica mesopore walls.
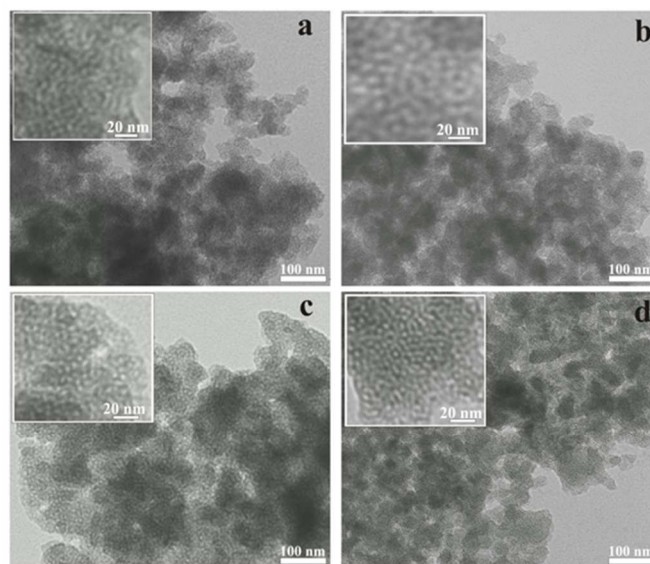

Fig. 1. TEM images of (a) Ce_{10}-Ni_{10}-UVM-7, (b) Ce_{60}-Ni_{10}-UVM-7, (c) Sn_{10}-Ni_{10}-UVM-7 and (d) Sn_{60}-Ni_{10}-UVM-7.

Table 1. Analytical and textural data for the Ce(Sn)$_y$-Ni$_x$-UVM-7 mesoporous supports.

Sample	Si/Ni[a]	Si/M[a]	Si/Ni[b]	Si/M[b]	S_{BET} (m^2/g)	Mesopore Size[c] (nm)	Mesopore Vol.[e] (cm^3/g)	Large pore Size[d] (nm)	Large pore Vol.[d] (cm^3/g)
Ni$_{60}$-UVM-7	60	-	78	-	1195	2.95	0.99	56.2	1.51
Ni$_{30}$-UVM-7	30	-	55	-	1061	2.92	0.99	53.3	0.88
Ni$_{10}$-UVM-7	10	-	42	-	1011	2.90	0.98	41.3	0..63
Ce$_{60}$-Ni$_{10}$-UVM-7	10	60	43	62	990	3.00	0.88	48.1	0.30
Ce$_{30}$-Ni$_{10}$-UVM-7	10	30	44	38	983	2.97	0.83	43.9	0.29
Ce$_{10}$-Ni$_{10}$-UVM-7	10	10	42	16	850	3.01	0.71	41.5	0.21
Sn$_{60}$-Ni$_{10}$-UVM-7	10	60	46	64	972	3.00	0.92	42.0	0.38
Sn$_{30}$-Ni$_{10}$-UVM-7	10	30	43	24	932	2.98	0.82	39.1	0.35
Sn$_{10}$-Ni$_{10}$-UVM-7	10	10	42	8	755	2.68	0.65	32.2	0.33

[a]Si/Ni, Si/Ce and Si/Sn molar ratio in the mother liquor. M= Ce or Sn. [b]Si/Ni, Si/Ce and Si/Sn molar ratio values in the solids from EPMA and ICP-OES. M= Ce or Sn. [c]Mesopore volume values and mesopore diameters calculated by using the BJH model on the adsorption branch of the isotherms for P/P$_0$ < 0.75. [d]Large textural-type pore volume values and diameters calculated by using the BJH model on the adsorption branch of the isotherms for P/P$_0$ > 0.75.

Table 2. Analytical and textural data for the Au/Ce$_y$-Ni$_x$-UVM-7 mesoporous catalysts.

Sample	Si/Ni[a]	Si/Ce[a]	Au[b] (wt.%)	Gold[c] (nm)	S_{BET} (m^2/g)	Mesopore Size[d] (nm)	Mesopore Vol.[d] (cm^3/g)	Large pore Size[e] (nm)	Large pore Vol.[e] (cm^3/g)
Au/Ni$_{10}$-UVM-7(200)	42	-	0.96	4.0±1.3	653	2.5	0.62	47.6	0.36
Au/Ce$_{60}$-Ni$_{10}$-UVM-7(200)	47	67	0.97	3.9±1.2	566	2.5	0.56	49.3	0.35
Au/Ce$_{30}$-Ni$_{10}$-UVM-7(200)	44	38	1.05	4.2±1.4	518	2.6	0.52	48.6	0.18
Au/Ce$_{10}$-Ni$_{10}$-UVM-7(200)	42	16	1.20	4.3±1.2	455	2.6	0.45	40.4	0.26
Au/Ni$_{10}$-UVM-7(500)	42	-	0.96	4.4±1.3	603	2.4	0.47	36.1	0.33
Au/Ce$_{60}$-Ni$_{10}$-UVM-7(500)	47	67	0.97	4.3±1.5	473	2.4	0.45	43.2	0.26
Au/Ce$_{30}$-Ni$_{10}$-UVM-7(500)	44	38	1.05	5.1±1.7	484	2.4	0.40	40.5	0.23
Au/Ce$_{10}$-Ni$_{10}$-UVM-7(500)	42	16	1.20	4.9±1.6	470	2.4	0.40	38.0	0.17

[a]Si/Ni and Si/Ce molar ratio values in the solids from EPMA and ICP-OES. [b]Percentage weight of gold determined by atomic absorption. [c]Gold particle size determined through HAADF. [d]Mesopore volume values and mesopore diameters calculated by using the BJH model on the adsorption branch of the isotherms for P/P$_0$ < 0.75. [e]Large textural-type pore volume values and diameters calculated by using the BJH model on the adsorption branch of the isotherms for P/P$_0$ > 0.75.

Table 3. Analytical and textural data for the Au/Sn$_y$-Ni$_x$-UVM-7 mesoporous catalysts.

Sample	Si/Ni[a]	Si/Sn[a]	Au[b] (wt.%)	Gold[c] (nm)	S_{BET} (m^2/g)	Mesopore Size[c] (nm)	Mesopore Vol.[c] (cm^3/g)	Large pore Size[d] (nm)	Large pore Vol.[d] (cm^3/g)
Au/Sn$_{60}$-Ni$_{10}$-UVM-7(200)	47	64	1.22	4.5±1.5	712	2.6	0.67	48.4	0.39
Au/Sn$_{30}$-Ni$_{10}$-UVM-7(200)	43	24	1.15	4.8±1.5	675	2.7	0.63	46.6	0.48
Au/Sn$_{10}$-Ni$_{10}$-UVM-7(200)	42	8	1.10	4.9±1.4	628	2.6	0.54	42.0	0.41
Au/Sn$_{60}$-Ni$_{10}$-UVM-7(500)	46	64	0.98	5.5±1.6	592	2.4	0.58	43.9	0.33
Au/Sn$_{30}$-Ni$_{10}$-UVM-7(500)	43	24	1.15	5.3±1.5	654	2.5	0.54	42.3	0.38
Au/Sn$_{10}$-Ni$_{10}$-UVM-7(500)	42	8	1.10	5.3±1.5	561	2.5	0.52	41.8	0.39

[a]Si/Ni and Si/Sn molar ratio values in the solids from EPMA and ICP-OES. [b]Percentage weight of gold determined by atomic absorption. [c]Gold particle size determined through HAADF. [d]Mesopore volume values and mesopore diameters calculated by using the BJH model on the adsorption branch of the isotherms for P/P$_0$ < 0.75. [e]Large textural-type pore volume values and diameters calculated by using the BJH model on the adsorption branch of the isotherms for P/P$_0$ > 0.75.

Catalysis Science & Technology Accepted Manuscript

The preservation of a certain bimodal porosity of our supports is further illustrated by N_2 adsorption-desorption isotherms (Fig. SI5). All curves show, a well-defined adsorption step at intermediate relative pressure ($0.2 < P/P_0 < 0.4$ range; corresponding to the filling of the intra-particle mesopores), and a second adsorption step, at a high relative pressure, due to the filling of the inter-particle large textural pores. The progressive reduction of this second adsorption step with the Ce and Sn content is related to the previously mentioned enhanced inter-particle condensation (with the subsequent decrease in the interparticle voids). As the heteroelement content increases, BET surface area and pore volume slightly decrease in a progressive way (see Table 1). On the other hand, the progressive incorporation of heteroelements practically does not affect the mesopore size of the final materials. Then, in the light of the results, all samples can really be considered as high surface area materials without significant pore blocking associated to the incorporation of oxidic nanoparticles.

Gold was incorporated through deposition precipitation in aqueous $HAuCl_4 \cdot 3H_2O$ solutions (2 %) using strictly the same protocol for all supports. In all cases, a similar proportion of inorganic anchors in the form of NiO_x domains exists (Si/Ni molar ratios in the 42-47 range) (Tables 2 and 3). The amount of gold incorporated increases in a gradual way from 0.96 to 1.20 (wt.%) with the Ce content. On the contrary, no clear evolution is observed dealing with the Sn containing materials. This behavior is probably due to the different zpc of CeO_2 (6.7-8.6) and SnO_2 (4.5-5). At the working pH (ca. 8-9), while a negative charge is expected for the SnO_2 surface, some residual positive charge will remains for the CeO_2 one. Then, as mentioned above, CeO_2 domains cooperate with NiO_x (zpc in the 10.3-11.1 range depending on the hydroxylation surface degree) acting both as effective anchors to interact with $Au(OH)_4^-$ anionic species. We have measured zpc values of 2.4, 2.7 and 2.9 for UVM-7, Ni_{10}-UVM-7 and Ce_{60}-Ni_{10}-UVM-7 supports, respectively. We observe an increase of the zpc value due to the presence of Ni and Ce as heteroelements. However, as the silica is the principal component in our composites, the presence of a relatively low proportion of NiO_2 and/or CeO_2 domains does not modify significantly the experimental zpc values. In any case, a certain local effect related to the zpc values of the different included oxides seems to be operative, which favor the adsorption of anionic gold complexes. On the other hand, the EDX analysis performed on the gold-containing catalysts allow us to discard the presence of Cl^- species which is consistent with the exhaustive washing mentioned above.

The treatment for gold incorporation does not alter in a qualitative way the UVM-7-like architecture at mesoscopic level. In fact, with the exception of the richest Sn material treated at 500ºC, all $Au/Ce(Sn)_y$-Ni_x-UVM-7 catalysts display low-angle XRD patterns (Fig. 3) with a signal or a shoulder associated with the (100) reflection. As observed in related systems, the intensity decrease of the (100) peak after gold inclusion must be attributed to a high phase-cancellation phenomenon associated with the introduction of scattering material (Au species) into the pore voids. The high-angle XRD patterns maintain the CeO_2 and SnO_2 peaks of the parent supports, but surprisingly, no signals attributed to metallic gold are observed (Fig. SI1 and SI2) regardless of the calcination temperatures used (200 or 500ºC). This fact is indicative of an extremely low particle size (< 5 nm) on the NiO_x or CeO_2 domains. The absence of XRD peaks associated with gold

particles also has been reported for Au/CeO_2 catalysts having very small Au crystalline domains and/or low gold concentration (< 1wt. %).[47]
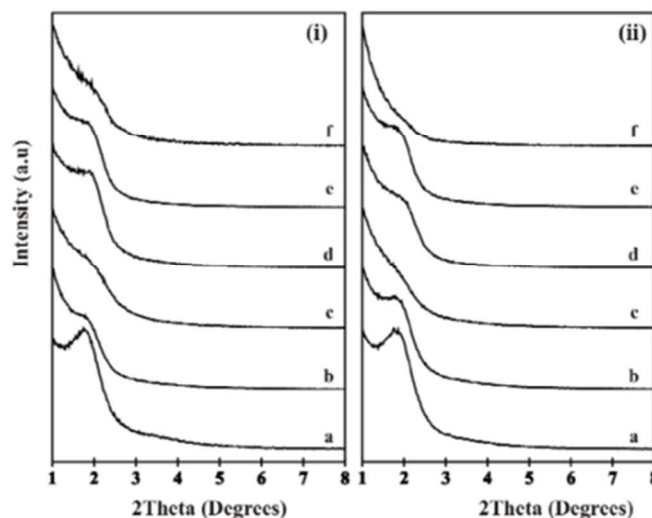
Fig. 2. Low-angle XRD patterns of the gold-containing catalysts processed at (i) 200ºC and (ii) 500ºC. (a) Au/Ce_{60}-Ni_{10}-UVM-7, (b) Au/Ce_{30}-Ni_{10}-UVM-7, (c) Au/Ce_{10}-Ni_{10}-UVM-7, (d) Au/Sn_{60}-Ni_{10}-UVM-7, (e) Au/Sn_{30}-Ni_{10}-UVM-7 and (f) Au/Sn_{10}-Ni_{10}-UVM-7.

According to the XRD analysis, Au/Ce_y-Ni_x-UVM-7 catalysts show similar TEM images of those of the parent gold-free $Ce(Sn)_y$-Ni_x-UVM-7 supports (Fig. 4 and 5). Apparently, there is no clear evidence on the gold incorporation from TEM images. At this point, only a low amount of white spots, probably ascribed to the largest gold particles, are detected by TEM. However, together with the chemical analysis, XEDS mapping supports not only the gold presence, but also the quality of the gold, nickel and ceria spatial distribution achieved in our catalysts treated at 200ºC (Fig. 3 and 4). A certain aggregation of Au and Ce(or Sn) is suggested by XEDS mapping carried out on samples calcined at 500ºC, as expected.

At this point, we record STEM-HAADF images of the gold-containing catalysts in order to achieve higher contrast between the gold nanoparticles and the silica-based support. Gold particles (white dots) are fairly uniformly distributed over the support (gray regions) (Fig. 5). Similar gold particle sizes (see Tables 2 and 3) and distributions have been obtained for Au/Ce_y-Ni_x-UVM-7 and Au/Sn_y-Ni_x-UVM-7 catalysts. The majority gold particles show an average size in the 3-5 nm range according to the particle size distribution histograms (Fig. 5). Moreover, a certain proportion of particles in the 5-7 nm range and even larger (ca. 20 nm) minority gold domains (according to TEM images in Figures 3 and 4) can be observed in the samples heated at 500ºC. This last behavior with temperature calcination is observed for all analyzed materials. Then, slightly larger mean particle sizes have been measured for samples treated at 500ºC when compared to catalysts processed at 200ºC. On the other hand, HRTEM allows us to detect individual gold crystalline nanoparticles in the solids processed at 500ºC (Fig. 6). These particles show a d spacing of 0.23 nm, typical of fcc Au,[48] measured on the image and confirmed through the FFT process. An average gold nanoparticle size in the 3-7 nm range has been determined through HRTEM. TEM analysis of Au-CeO_2 and Au-UVM-7 catalysts indicated larger gold particles, ie 5-11 nm.[43, 44] This

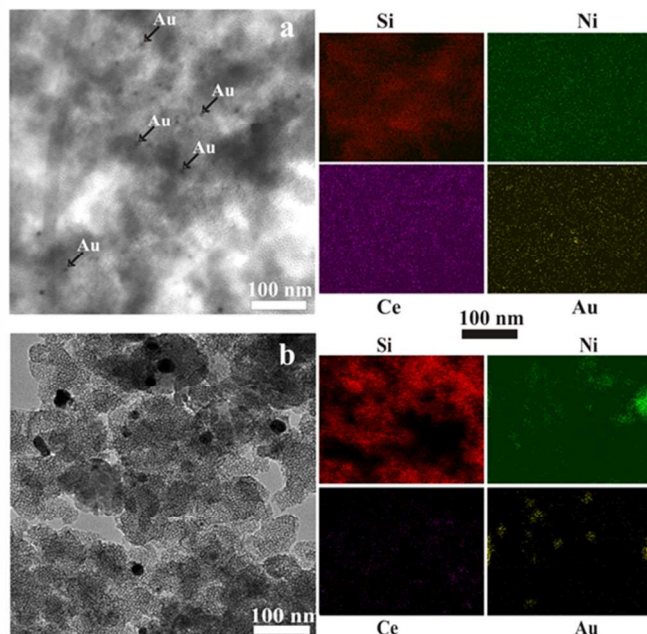small size of the gold domains is consistent with the absence of XRD signals as discussed above.

Fig. 3. TEM and XEDS mapping of Au/Ce$_{10}$-Ni$_{10}$-UVM-7 catalyst treated at (a) 200ºC and (b) 500ºC.
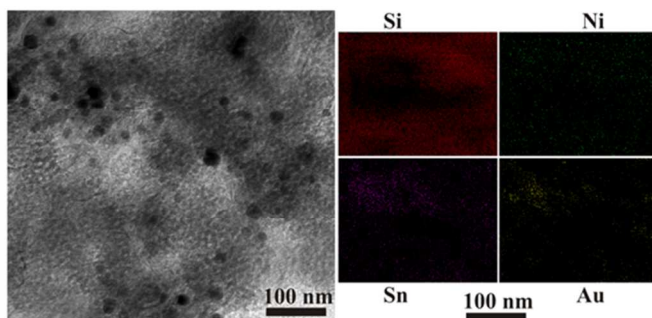

Fig. 4. TEM and XEDS mapping of Au/Sn$_{10}$-Ni$_{10}$-UVM-7 catalyst treated at 500ºC.

The mesophase and porosity preservation after gold incorporation is further supported by N$_2$-adsorption–desorption isotherms (Fig. 7 and 9). Regardless the calcination temperature, all solids maintain the two adsorption steps reminiscent of the UVM-7 silica (though somewhat lower). The BJH pore size distributions show a first peak at mesopore sizes in the 2-3 nm range and a second signal without a definite maximum (large textural pores) (Fig. SI5-8). These features indicate that the simultaneous incorporation of Ni and Ce(or Sn) together with the pH conditions used for the gold incorporation favor the interparticle condensation through the formation of Si-O-Si, Si-O-M and M-O-M bonds (M= Ni, Ce or Sn). Moreover, we observe a decrease in the adsorption capacity at high pressure for samples treated at 500ºC. This suggests that additional inter-particle condensation is favored at higher temperature, as expected. In any case, all catalysts present high surface areas and pore volumes (Tables 2 and 3). In each series, the BET area and pore volume values slightly decrease with the Ce or Sn content (the nickel content can be

considered as constant: 42 < Si/Ni < 47). This effect is more pronounced in the case of the Ce-containing catalysts, and could be tentatively attributed to the relatively greater size of the CeO$_2$ domains when compared to the SnO$_2$ (according to XRD). Obviously, the gold incorporation leads to a significant BET area and pore volume decrease when compared to those parameters of the respective parent gold-free supports. Finally, dealing with the mesopore size, no significant changes are observed for each family. This is an expected behavior as no appreciable mesopore size changes were previously observed for the gold-free supports with the Ni, Ce and Sn content. However, two general tendencies can be mentioned: (a) BJH mesopore sizes decreases from *ca.* 3 to 2.5 nm after gold incorporation (due the inclusion of Au species inside the mesopores), and (b) an additional pore size decrease from *ca.* 2.5 to 2.3-2.4 nm occurs when samples were processed at 500ºC (this effect seems to be related with silica condensation processes).
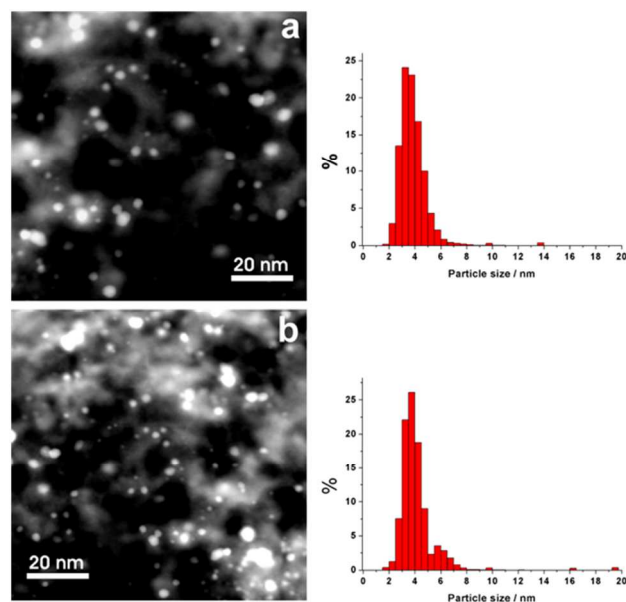

Fig. 5. STEM-HAADF images and gold particle size distribution histrograms of Au/Ce$_{60}$-Ni$_{10}$-UVM-7 catalyst (a) treated at 200ºC, and (b) treated at 500ºC.
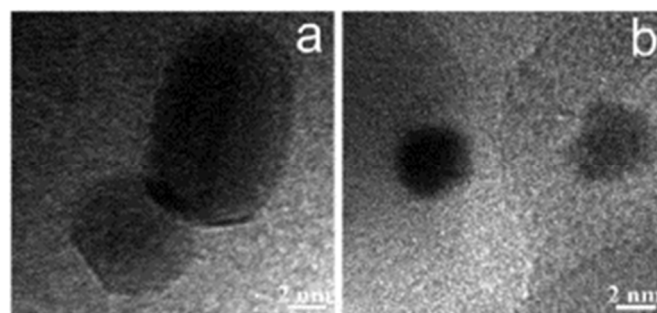

Fig. 6. HRTEM images of (a) Au/Ce$_{10}$-Ni$_{10}$-UVM-7 and (b) Au/Sn$_{10}$-Ni$_{10}$-UVM-7 catalysts treated at 500ºC and showing isolated gold nanoparticles.
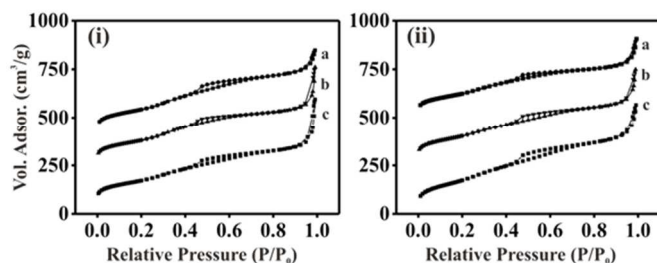
Fig. 7. N$_2$ adsorption desorption isotherms of catalysts (a) Au/Ce$_{10}$-Ni$_{10}$-UVM-7, (b) Au/Ce$_{30}$-Ni$_{10}$-UVM-7 and (c) Au/Ce$_{60}$-Ni$_{10}$-UVM-7, processed at (i) 200ºC and (ii) 500ºC.
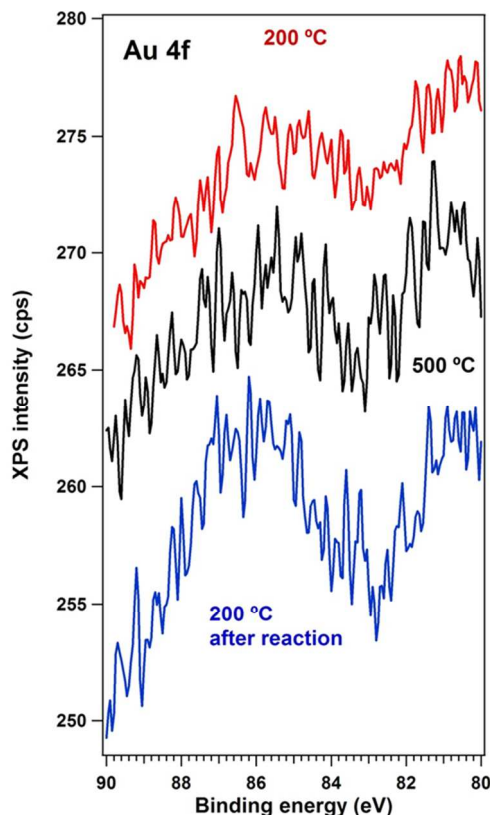
Fig. 8. XPS spectra of Au/Ce$_{10}$-Ni$_{10}$-UVM-7(200) and Au/Ce$_{10}$-Ni$_{10}$-UVM-7(500) samples in the region of Au 4f level.

XPS spectra corresponding to fresh and tested Au/Ce$_{60}$-Ni$_{10}$-UVM-7(200) and Au/Ce$_{60}$-Ni$_{10}$-UVM-7(500) catalysts are presented in Figures 8-10. In addition Table 4 compiles the binding energies of Au4f, Ce3d, Ni2p3/2, O1s and N1s levels for the series of Ni-, Au-Ni-, Ce-Ni- and Au-Ce-Ni- catalysts. Typically, the main components of Au 4f7/2 peaks corresponding to the presence of gold in metallic state are centered at binding energies around 84.2 eV,[41] while higher than 84.5 eV indicate the presence of the electropositively charged Au states. Although the signal-to-noise ratio is very low due the very small content and high dispersion of gold, the binding energies measured in Figure 10 denote for the investigated catalysts, according to the literature data, only the presence of oxidized Au species (Table 4).[49] For the spent samples no evident change occurred in the oxidation state of

gold. However, the very low signal-to-noise ratio does not allow a comparison of the atomic XPS and analytic Au/Si ratios as a function of the catalysts composition or of the calcination temperature
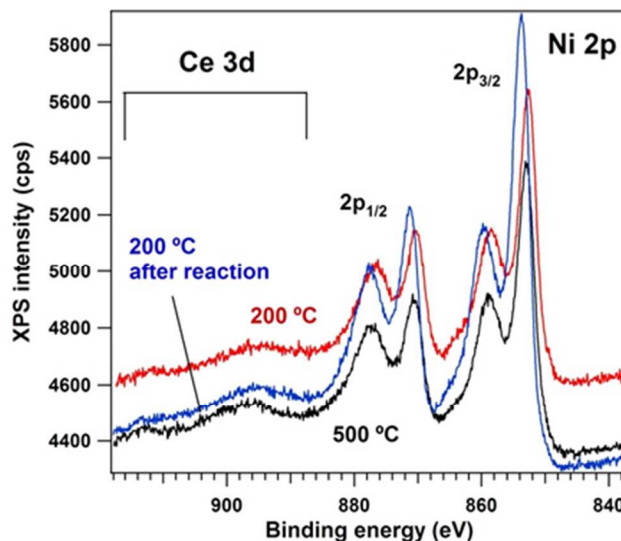
Fig. 9. XPS spectra of Au/Ce$_{10}$-Ni$_{10}$-UVM-7(200) and Au/Ce$_{10}$-Ni$_{10}$-UVM-7(500) samples in the region of Ce 3d and Ni 2p levels.
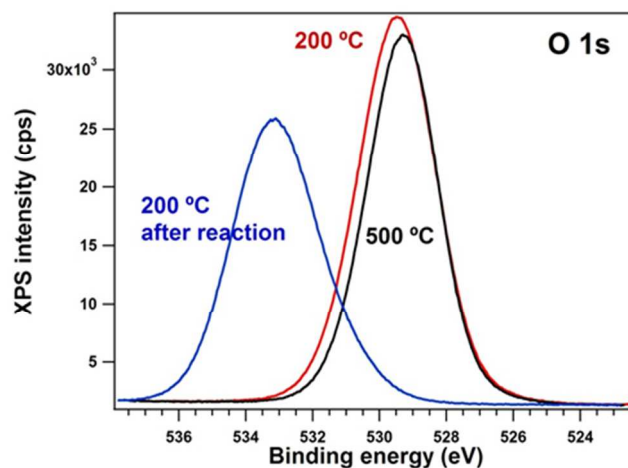
Fig. 10. XPS spectra of Au/Ce$_{60}$-Ni$_{10}$-UVM-7(200) and Au/Ce$_{60}$-Ni$_{10}$-UVM-7(500) samples in the region of O 1s level.

Table 4. XPS binding energies of Au4f, Ce3d, Ni2p3/2, O1s and N1s levels and composition for Ni_x-, Ni_x-Ce_y-, and Au-Ni_x-Ce_y-UVM-7 catalysts.

Catalyst	XPS level Binding energy, eV					Atomic Au/Si ratio x 10^3	
	$Au4f_{7/2}$	$Ce3d_{5/2}$/ $Ce3d_{5/2}$ shake up	$Ni2p_{3/2}$	O1s	N1s	XPS	Analytic
Ni_{60}-*	-	-	852.5	529.3	-	-	-
Ni_{30}-*	-	-	852.4	529.2	-	-	-
Ni_{10}-*	-	-	852.3	529.4	-	-	-
Ce_{60}-Ni_{10}-*	-	882.4/916.1	852.4	529.5	-	-	-
Ce_{30}-Ni_{10}-*	-	881.9/915.6	852.3	529.4	-	-	-
Ce_{10}-Ni_{10}-*	-	882.1/915.8	852.4	529.3	-	-	-
Au/Ni_{10}-*	86.0	-	852.5	529.4	-	3.4	3.1
Au/Ce_{60}-Ni_{10}-*	86.1	882.3/916.0	852.5	529.5	-	3.5	3.2
Au/Ce_{60}-Ni_{10}-***	86.2	882.5/916.2	853.7	533.1	-	3.5	3.2
Au/Ce_{30}-Ni_{10}-*	86.1	882.2/915.9	852.6	529.3	-	3.8	3.6
Au/Ce_{10}-Ni_{10}-*	86.2	882.3/916.0	852.6	529.2	-	4.3	4.5
Au/Ni_{10}-**	86.1	-	853.8	533.2	-	3.9	3.1
Au/Ce_{60}-Ni_{10}-**	86.2	882.3/916.0	853.9	533.3	-	4.0	3.2
Au/Ce_{30}-Ni_{10}-**	86.1	882.4/916.1	853.8	533.2	-	4.3	3.6
Au/Ce_{10}-Ni_{10}-**	86.1	882.2/915.9	853.8	533.2	-	5.02	4.5

*-calcined at 200 °C; **-calcined at 500 °C; ***-calcined at 200 °C after reaction

Table 5. Performances of the multicomponent catalysts in aerobic oxidative condensation of benzylamine to N-benzylidenbenzilimine.

Entry	Catalyst	Conversion (%)		Selectivity (%)	Productivity ($mol_{product}$ g_{cat}^{-1} h^{-1})		TOF 4h
		75°C	115°C		75°C	115°C	115°C
1	Blank experiment*	4.8	6.1	87**			
2	Ni_{10}-UVM-7	7.4	9.2	100	2.12	2.64	
3	Ni_{30}-UVM-7	6.9	8.6	100	1.40	1.75	
4	Ni_{60}-UVM-7	6.2	7.4	100	0.96	1.15	
5	CeO_2	5.6	-	100	0.03	-	
6	Ce_{60}-Ni_{10}-UVM-7	43.6	47.5	100	2.81	3.05	
7	Ce_{30}-Ni_{10}-UVM-7	41.6	46.9	100	1.61	1.82	
8	Ce_{10}-Ni_{10}-UVM-7	39.8	43.9	100	1.04	1.15	
9	Sn_{60}-Ni_{10}-UVM-7	16.2	22.7	100	1.17	1.64	
10	Sn_{30}-Ni_{10}-UVM-7	15.8	20.9	100	0.60	0.80	
11	Sn_{10}-Ni_{10}-UVM-7	14.8	20.0	100	0.26	0.35	
12	Au/Ni_{10}-UVM-7(200)	30.1	41.8	100	3.52	4.89	
13	Au/Ni_{10}-UVM-7(500)	28.8	39.4	100	3.37	4.61	
14	Au-UVM-7	4.9	6.5	100	2.10	2.78	456
15	Au-CeO_2	18.5	23.7	100	2.08	2.67	458
16	Au/Ce_{60}-Ni_{10}-UVM-7(200)	71.5	99.4	100	4.04	5.62	919
17	Au/Ce_{30}-Ni_{10}-UVM-7(200)	65.4	94.2	100	2.33	3.36	805
18	Au/Ce_{10}-Ni_{10}-UVM-7(200)	62.0	88.7	100	1.51	2.16	662
19	Au/Ce_{60}-Ni_{10}-UVM-7(500)	58.7	81.6	100	3.31	4.61	754
20	Au/Ce_{30}-Ni_{10}-UVM-7(500)	55.6	76.2	100	1.98	2.72	651
21	Au/Ce_{10}-Ni_{10}-UVM-7(500)	51.1	71.5	100	1.24	1.74	534
22	Au/Sn_{60}-Ni_{10}-UVM-7(200)	47.2	59.2	100	2.86	3.59	435
23	Au/Sn_{30}-Ni_{10}-UVM-7(200)	44.7	54.7	100	1.55	1.90	426
24	Au/Sn_{10}-Ni_{10}-UVM-7(200)	41.7	53.5	100	0.70	0.90	435
25	Au/Sn_{60}-Ni_{10}-UVM-7(500)	44.1	58.4	100	2.67	3.54	429
26	Au/Sn_{30}-Ni_{10}-UVM-7(500)	41.2	53.4	100	1.43	1.85	416
27	Au/Sn_{10}-Ni_{10}-UVM-7(500)	39.8	50.5	100	0.67	0.85	411

Reaction time: 4h; *-24h; **-secondary product : benzaldehyde.

Catalysis Science & Technology Accepted Manuscript

The calcination at 500 $^{\circ}$C and the exposure to reaction also caused an oxidation of nickel as it has been evidenced from the values of the Ni2p$_{3/2}$ and 2p$_{1/2}$ energy levels for the investigated catalysts (Figure 9, Table 4).[50] These values demonstrate that for nickel both the thermal treatment and especially the exposure to the reaction led to an oxidation of the metal (for Au/Ce$_{60}$-Ni$_{10}$-UVM-7(200): BE of 852.5 and 858.4 eV, for Au/Ce$_{60}$-Ni$_{10}$-UVM-7(500): BE of 853.9 and 859.8 eV, and for the spent Au/Ce$_{60}$-Ni$_{10}$-UVM-7(200): BE of 853.7 and 859.7 eV. A certain aggregation is also suggested by Figure 9 for Ni. Also, an important shift of the binding energy was determined for the O 1s level after reaction (for Au/Ce$_{60}$-Ni$_{10}$-UVM-7(200): BE of 529.5 eV, for Au/Ce$_{60}$-Ni$_{10}$-UVM-7(500): BE of 529.3 eV, and for the spent Au/Ce$_{60}$-Ni$_{10}$-UVM-7(200): BE of 533.1 eV) (Figure 10). This indicates that an evolution occurs in the surface oxygen species during the catalytic process from lattice to electrophilic oxygen (O$^-$, O$_2^-$) probably related to the formation of metal-OH bonds and the generation of anionic defects in the oxygen lattices.[51, 52] This evolution is consistent with the catalyst nature (amorphous and easily hydroxilated silica-based walls, and cerium oxide domains able to cycle easily between Ce^{3+} and Ce^{4+} with the subsequent oxygen transport) and the catalytic process (benzylamine oxidation). In addition, for the spent catalyst no band assigned to N 1s was detected. No change in the position and the intensity of the bands assigned to Ce 3d (Figure 9, Table 4) or Si 2p (for Au/Ce$_{60}$-Ni$_{10}$-UVM-7(200): BE of 103.4 eV, for Au/Ce$_{60}$-Ni$_{10}$-UVM-7(500): BE of 103.6eV, and for the spent Au/Ce$_{60}$-Ni$_{10}$-UVM-7(200): BE of 103.5 eV) was detected in these measurements. Obviously, the presence of the peak in the region 913 eV or at higher energies is a proof for the presence of Ce^{4+} species.[53] Replacing cerium by tin or compositional changes does not alter the tendencies observed for the XPS spectra of Au/Ce$_{60}$-Ni$_{10}$-UVM-7 catalysts.

3.2. Catalytic tests

Previous work of Corma and Garcia[28] using gold supported on various supports demonstrated that while the selectivity was almost not influenced by the metal loading that implicitly meant particle size, the conversion of benzylamine to the desired imine was strongly influenced. In the series these authors have been investigated the nature of the support was less important.

Although in a small extent, blank experiments showed this reaction proceeds, indeed with the formation of a secondary product (benzaldehyde), even in the absence of the catalyst (Table 4, entry 1). Metal-free oxidation of benzyl amines to imines was also recently reported working with oxygen[54] or with hydrogen peroxide.[55] Like in our case the selectivity to imine was partial. A very similar result was obtaining using pure siliceous UVM-7 support. CeO$_2$ oxide led to a very small conversion and productivity, but again the reaction occurred selectively to imine (Table 5).

Previous reports working with gold indicated that for this reaction the support nature has a relatively low influence, more important being the size of the metal particles.[7] Here we have firstly compared the activity of a Au-UVM-7 catalyst (Table 5, entry 14) with that of a supported Au/CeO$_2$ (Table 5, entry 15), the first one prepared by embedding Au colloids, and the second by impregnation of a cerium oxide support. Both catalysts exhibited comparative gold particle sizes (4 nm). Data presented in the Table 5 (entries 14 and 15) showed that the two catalysts had comparable productivities. Hence, the relatively

small influence of the support nature was indeed re-confirmed for single oxide supports like CeO$_2$, SiO$_2$.

The experiments carried out in the presence of the new multicomponent catalysts also led selectively to N-benzylidenbenzylamine. However, important differences in the activity expressed as productivity were determined as a function of the composition (Table 5).

In order to verify the role played by the different included/deposited heteroelements, we have studied the catalytic behavior in a sequential way from mono- to multicomponent (Ce, Sn, Ni) containing materials to catalysts in which these materials served as supports for gold. As mentioned the results were presented in terms of productivity. Data compiled in the Table 5 were collected after 4h reaction and the reason was to compare at the same reaction time catalysts with different activities. It is important to mention that i) all the presented data were collected before the conversion reached a plateau, ii) the reaction was not affected by mass transfer limitations in these experiments as confirmed by Koros-Novak criterion (slope ln r/ ln f$_m$ close to 1),[56] and iii) productivities calculated at very short reaction times (less than 10 min) had the same values with those presented in Table 5.

Nickel oxide entrapped in the UVM-7 structure presented productivities in the range 0.96 – 2.12 mol$_{product}$ g$_{cat}^{-1}$ h^{-1} at 75 $^{\circ}$C and 1.15 – 2.64 at 115 $^{\circ}$C showing a linear dependence with the nickel content. The addition of the second heteroelement led to a different behavior. Thus, the addition of tin oxide caused a decrease in the productivities (Table 5, entries 9-11), while cerium oxide induced an increase of the productivities to 40% (Table 5, entries 6-8).

As compared to Ni$_{10}$-UVM-7, Ce$_x$-Ni$_{10}$-UVM-7 or Sn$_x$-Ni$_{10}$-UVM-7 the addition of gold led to an increase of the productivity irrespective of the nature of the support (Table 5, entries 12-14 and 16-27) that is in a full agreement with previous reported data on the role of gold in this reaction.[4, 17, 27, 57] However, the increase was more evident when the supports contain Ni or a combination of the Ce and Ni as heteroelements (Table 5, entries 12-13 and 16-21). Thus, in the case of the Au/Ce$_{60}$-Ni$_{10}$-UVM-7(200) catalyst the productivity was of 4.04 and 5.62 mol$_{product}$ g$_{cat}^{-1}$ h^{-1} at 75 and 115 $^{\circ}$C, respectively. Such a catalyst corresponds to a Si/Ce ratio of 60 and Si/Ni ratio of 10. These results may account for a more advanced interaction of gold with nickel. More evident arguments that the direct interactions Au/Ni are beneficial are provided by the Au/Ni$_{10}$-UVM-7(200) catalyst. It was almost as active as the Au/Ce$_{60}$-Ni$_{10}$-UVM-7(200) catalyst (Table 5). Changes in the activity with the atomic ratios of the constitutive elements may also support this affirmation. Thus, higher loadings of Ce or Sn led to a decrease of productivity, showing a less effective interaction with gold.

Since the deposition of gold onto UVM-7 including different heteroelements took place in an alkaline solution followed by a calcination step at 200 or 500 °C, these materials were separately treated following the same procedure in order to determine if such a treatment may exhibit an influence on the catalytic behavior. However, the experiments indicated no real differences between pre-calcined and non-calcined materials. But the calcination of the Au containing catalysts at 500ºC corresponded to a decrease in the productivity irrespective of the catalyst composition as compared to samples calcined at 200ºC that has been correlated to the increase of the metal particle size, typically occurring for temperatures higher than 500 $^{\circ}$C (Tables 2 and 3).[51] According to Guirrane et al.,[7, 28] a significant increase in the number of unsaturated gold atoms

(probably the active sites) must occur when decreasing the gold crystal size.

Concluding, data presented in Table 5 indicate that for more complex supports like multi- heterocomponent Ce(Sn)$_y$-Ni$_x$-UVM-7 oxides (as demonstrated by XPS) the support is not a simple spectator. A very high surface area (typical of M41s materials) in addition to an improved accessibility (as occurs for UVM-7-like silicas) can be correlated in the case of the entrapped metal catalysts with a better dispersion of the active species. Such a behavior has a direct influence on the productivity of these catalysts. These data also demonstrate that in addition to the support architecture (at mesoscale) the local organization and nano dispersion of anchors, promoters and catalytic sites is very important. The inclusion of inorganic anchors and promoters must be considered as efficient assembly tools to improve the "cooperative properties" of our catalysts. The final effect associated with the support design and selection of heteroelements results in a better dispersion of gold nanoparticles. Thus, the Ce content does not significantly affect the size of the gold nanoparticles. We have observed similar dispersions of Ni, Ce and Au for samples with varying amount of Ce (see TEM Figures 3-5, and comments on that). CeO$_2$ appears to act as an inorganic anchor. The Au content increased somewhat with that of Ce. Even changing the metal, *ie* cerium with tin, does not affect the size of the gold nanoparticles under our working conditions. However, data presented in Table 5 show that the gold particle size is not the only parameter of influence on the catalytic efficiency. Hence, we observe different values of the productivity (entries 12-13 and 16-27) when the chemical composition of the support changes (maintaining the average size for the gold domains).

The performances of the new multicomponent Au catalysts (Table 5) are very close to those reported in the literature for gold supported catalysts on titania[7] but higher than those reported for gold deposed on ceria.[15] This is also valuable for the reference Au-CeO$_2$ catalyst (Table 5, entry 15) and Au-UVM-7 (Table 5, entry 14). Taking into account that the proposed active catalytic sites for the benzylamine oxidation are unsaturated gold atoms located at the particle corners and/or the interphases,[7, 22] a decrease in the gold nanoparticle size should be considered as a beneficial aspect. The average gold particle size in our catalysts is around 4 nm for Au deposed on Ce$_y$-Ni$_x$-UVM-7, and 4.5-5 nm for Au deposed on Sn$_y$-Ni$_x$-UVM-7, this leading to high conversions for Au/Ce$_y$-Ni$_x$-UVM-7 mesoporous materials. These values are in good accordance with previous data in the bibliography on Au-TiO$_2$ solids (gold particle size and TOF values of 3.5 nm and 70 h^{-1}, respectively).[7] Then, the activities of Au-UVM-7 (TOF 456 h^{-1}) and Au-CeO$_2$ (TOF 458 h^{-1}) catalysts (entries 14 and 15 in Table 5) must be also associated with the gold particle size (around 4 nm). Since the XPS data do not show important differences in the oxidation state of gold onto the different supports, it results that, indeed, the particle size is the main factor controlling the activity of Au in this reaction.

Figure 11 shows the variation of the conversion in time on Ni-, Au-Ce, and Au-Ce,Ni-UVM-7 catalysts. A continuous conversion increase in time till around 3h was observed for all the catalysts.

Kinetic studies carried on gold powder-catalyzed reaction by Lazar and Angelici showed that the rate of this reaction is independent of the O$_2$ concentration/pressure.[14, 58] Experiments carried out at different oxygen pressures with Au/Ce$_{60}$-Ni$_{10}$-UVM-7(200) and Au/Ce$_{30}$-Ni$_{10}$-UVM-7(200) catalysts showed an increase of the conversion till the pressure reach 5 atm

(Figure 12). Further increase of the oxygen pressure above 5 atm accounted to the results of Lazar and Angelici.[14, 58] No changes in the selectivity or reaction products have been evidenced under these conditions..
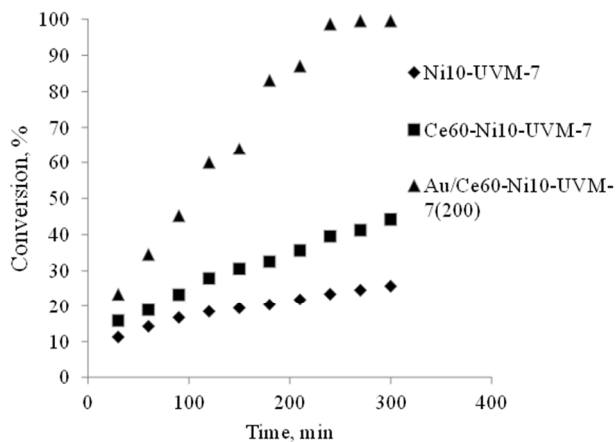

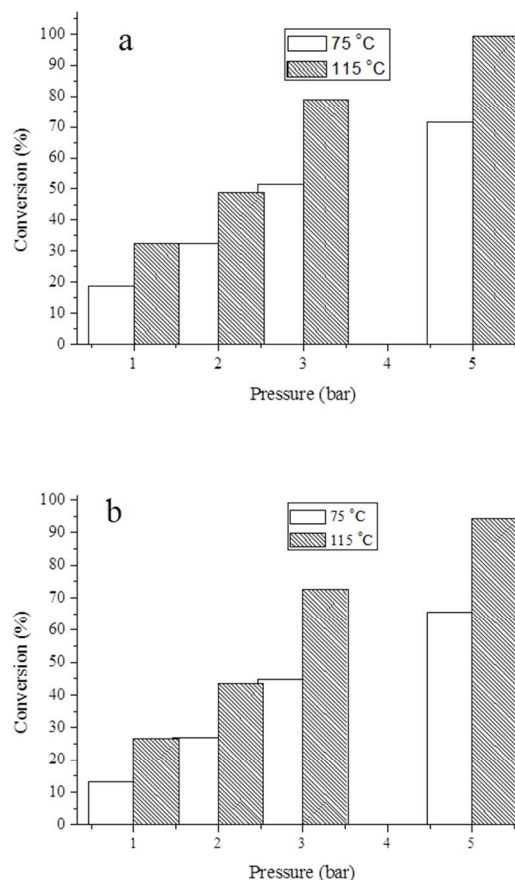**Fig. 11**. The variation of the conversion in time on Ni-, Au-Ce, and Au-Ce,Ni-UVM-7 catalysts.

Fig. 12. Conversion of benzylamine on Au/Ce$_{60}$-Ni$_{10}$-UVM-7(200) (a) and Au/Ce$_{30}$-Ni$_{10}$-UVM-7(200) (b) under different pressures of oxygen after 4h.

Activation of molecular oxygen on gold was reported to depend on both size and environments. Corma and the co-workers indicated that gold nanoparticles act as a bifunctional catalyst able to dissociate molecular oxygen on unsaturated atoms to generate oxygen reactive species and also to activate the organic substrate at the same time.[59-61] The presence of an additional element in the close proximity of gold may also affect the activation of oxygen. Thus, periodic density functional theory calculations investigating the effect of doping a gold model surface with Ni showed that this transitional element may stabilize the adsorbate–surface interactions with a concomitant decrease of the activation energy barriers for the oxygen dissociation to values that are smaller than the adsorption energies of molecular oxygen on gold.[62] These findings are in line with our results showing an improvement of the activity when gold nanoparticles were supported on Ni and Ce oxide nanodomains partially embedded inside the mesoporous UVM-7 silica walls. These catalysts were superior to those supported on Sn or large loadings of Ce oxide nanodomains inside the same mesoporous UVM-7 silica walls.

Thus, it appears that the new catalysts we proposed in this study bring together advantages that recommend them as effective in selective oxidation of benzylamine to N-benzylidenbenzylamine: ie stabilized Ni and Ce oxide nanodomains by partially embedding inside the mesoporous UVM-7 silica walls that activate gold nanoparticles. These particularities are in line with recent suggestions of Stowers et al.[63] indicating that stabilization methods of active gold particles may include partially coating the surface of the material, and the use of metal oxides in interaction with the catalyst.

On bulk gold, reports indicated that molecular oxygen can be activated via a hydroperoxyl (OOH) intermediate produced by abstracting a hydrogen atom from substrate or water, and the fact that extra water molecules significantly promote the hydrogen-transfer reactions, lowering the activation barrier of OOH formation.[62] On the other side, on these surfaces molecular oxygen is suggested to dissociate to form the active oxygen species that generates a reaction site, which selectively activates the substrate leading to OH groups. Hydroxyls formed on the surface rapidly disproportionate to form water.[64]

These achievements may confirm our results indicating that the role of water is important in systems containing Au particles. In addition, in our system water is also a substrate participating in the hydration of aldimine. The addition of water as 1-20 µL to the catalysts described in entries 12-13 and 16-27, was found to influence the activity but without any effect on selectivity. To check in more details the effect of water, experiments with dried benzylamine, methanol and oxygen have been carried out as well. Compared to the case where non-dried reactants have been used the reaction in which dried reactants were tested required an induction period (Table 6, entries 1 and 7). Thus, it varied from around 30 min for Au/Ce$_{60}$-Ni$_{10}$-UVM-7(200) and Au/Ce$_{30}$-Ni$_{10}$-UVM-7(200) till 50 min for Au/Sn$_{30}$-Ni$_{10}$-UVM-7(500) and Au/Sn$_{10}$-Ni$_{10}$-UVM-7(500). The supplementary addition of 10 µL water to the reaction system caused an increase of productivity from 4.04 (Table 5, entry 16) till 4.62 mol$_{product}$ g$_{cat}^{-1}$ h^{-1} (Table 6, entry 5) for the Au/Ce$_{60}$-Ni$_{10}$-UVM-7(200) catalyst. A similar behavior was determined for Au/Ce$_{30}$-Ni$_{10}$-UVM-7(200) (Table 5, entry 17, and Table 6, entries 8-12).

Then, benzaldehyde was considered in many examples as a key intermediate.[23, 65] The produced benzaldehyde was suggested to react with the excess benzylamine to form benzylidene benzylamines resulting in the final product for the benzylamine self-coupling reactions. To confirm this behavior we have carried out experiments on the same Au/Ce$_{60}$-Ni$_{10}$-UVM-7(200) and Au/Ce$_{30}$-Ni$_{10}$-UVM-7(200) catalysts by introducing benzaldehyde in the reaction mixture. Compared to the results presented in the Table 5, on these catalysts the conversion was total even at 75 °C after 2h (productivities of 5.65 and 3.57 mol$_{product}$ g$_{cat}^{-1}$ h^{-1}, respectively). This fact confirms that, indeed, the addition of benzaldehyde modifies the dynamics of the product formation. In fact, in the range of investigated benzylamine/benzaldehyde molecular ratios (from 5:1 to 1:1), benzaldehyde was detected in the reaction product only for the 1:1 benzylamine/benzaldehyde ratio, in 9% and 12% for samples Au/Ce$_{60}$-Ni$_{10}$-UVM-7(200) and Au/Ce$_{30}$-Ni$_{10}$-UVM-7(200), respectively.

Based on the experimental evidences we collected in this study the following reaction mechanism has been re-confirmed (Scheme 2).[17] Although not detected, the oxidative dehydrogenation of benzylamine, giving the aldimine is assumed as a first step of reaction (Scheme 2 (1)). It may also occur as a single-electron oxidation catalyzed by nano-gold particles[28] deposed on Ni and Ce (or Sn) oxide nanodomains partially embedded inside the mesoporous UVM-7 silica walls. It occurs via the intermediate (A) that generates aldimine and water. Then, hydrolysis of the aldimine occurs as a second step (Scheme 2 (2)), where ammonia is released and benzaldehyde is generated. Finally, benzaldehyde suffers a condensation with benzylamine leading to N-benzylidenbenzylamine (Scheme 2 (3)). It is worth to note that in the presence of oxygen smaller benzylamine/benzaldehyde ratios than 1:1 do not inhibit the steps 1 and 2 but only increase the amount of non-reacted benzaldehyde.

Among the elements included in the new multicomponent catalysts gold is more favorite in this reaction as active site because, as opposed to nickel, tin or even cerium oxides it can easily release oxygen. XPS showed that nickel is, however, irreversible oxidized. As shown from the productivity values silica embedded nickel nanoxides is also a valuable catalyst. In addition, silica embedded nickel nanoxides in connection with silica embedded cerium nanoxides also provide excellent nano-supports for gold. As a support to this conclusion, XPS analysis revealed that for gold, although the thermal treatment and exposure to the reaction determined a slight agglomeration, it preserved its oxidation state along ten catalytic cycles.

Figure SI9 shows the evolution of the conversion for the ten cycles for two Au/multicomponent supports catalysts. No change in the conversion was determined under these conditions. However, the results included in this figure were collected from experiments performed at high conversions which may not prove good recyclability. Therefore we completed these tests with results collected at lower conversions (Figure SI10). Indeed, they confirmed the recyclability of the catalysts. This has also been confirmed by ICP-OES analysis of the reaction products checking for Au, and by the characterization of the catalysts using the techniques described above. As it results from the Scheme 2, on the basis of the analytic measurements, ammonia is a by-product of this reaction. It is important to note that none of the investigated catalysts has been deactivated by ammonia, and their re-use led to similar conversions. In addition, XPS spectra of the spent catalysts did not show the presence of nitrogen that is an additional confirmation of the stability of these catalysts.
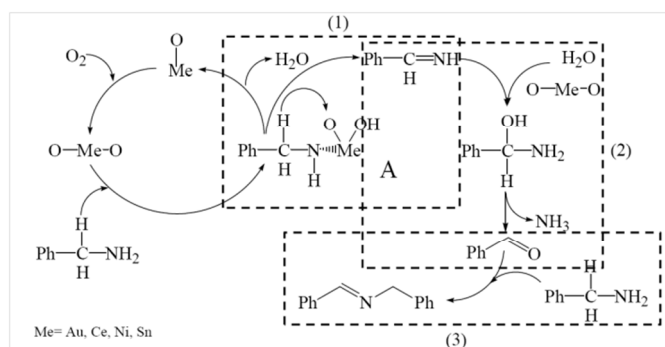
Scheme 2. Mechanism of the aerobic oxidative condensation of benzylamine to N-benzylidenbenzilimine

Table 6. The effect of water on performances of the multicomponent catalysts in aerobic oxidative condensation of benzylamine to N-benzylidenbenzilimine

Entry	Catalyst	Additional water (μL)	Conversion (%)	Selectivity (%)	Productivity ($mol_{product} \, g_{cat}^{-1} \, h^{-1}$)
1	Au/Ce$_{60}$-Ni$_{10}$-UVM-7(200)	dried reactants*	62.4	100	1.76
2	Au/Ce$_{60}$-Ni$_{10}$-UVM-7(200)	1.0	73.5	100	4.15
3	Au/Ce$_{60}$-Ni$_{10}$-UVM-7(200)	2.0	78.4	100	4.43
4	Au/Ce$_{60}$-Ni$_{10}$-UVM-7(200)	5.0	81.2	100	4.58
5	Au/Ce$_{60}$-Ni$_{10}$-UVM-7(200)	10.0	81.7	100	4.62
6	Au/Ce$_{60}$-Ni$_{10}$-UVM-7(200)	20.0	80.6	100	4.55
7	Au/Ce$_{30}$-Ni$_{10}$-UVM-7(200)	dried reactants*	53.2	100	0.94
8	Au/Ce$_{30}$-Ni$_{10}$-UVM-7(200)	1.0	68.4	100	2.33
9	Au/Ce$_{30}$-Ni$_{10}$-UVM-7(200)	2.0	72.7	100	2.60
10	Au/Ce$_{30}$-Ni$_{10}$-UVM-7(200)	5.0	75.0	100	2.68
11	Au/Ce$_{30}$-Ni$_{10}$-UVM-7(200)	10.0	75.1	100	2.68
12	Au/Ce$_{30}$-Ni$_{10}$-UVM-7(200)	20.0	72.8	100	2.60

Temperature 75 °C; Reaction time: 4h; *-required an induction period of 4h; **-results collected after 8h

4. General assessments

The success of the supported catalysts depended on a variety of key parameters affecting both the support nature and the design of the individual catalytic site. But this is not enough, and in most cases a regular and homogeneous distribution of the catalytic centers is required. This last aspect, dealing with the spatial distribution at the nanoscale, must be viewed as a collective property of the catalytic sites considered as a whole, as has been nicely discussed in a recent paper.[42] Dealing with catalysts based on metal nanoparticles inside mesoporous materials, in addition to a good selection of the support, nanoparticle assembly tools are usually required in order to tune and control the "cooperative properties" of the nanoparticles.

While there is no doubt about the esthetic appeal of symmetry, it was also argued that a periodic and ordered unimodal mesoporous support could not offer specific advantages for catalytic applications requiring an enhanced accessibility to the active sites and easy diffusion of reagents and products.[66] Then, we have selected as support the disordered UVM-7 porous silica, with a topology constructed by aggregation of mesoporous primary nanoparticles defining large inter-particle pores.[38, 39, 67] This architecture leads to 3D interconnected and tortuous mesopores having nanometric lengths. These features favor the accessibility to the active sites and prevents the undesirable migration and growing of metal nanoparticles.[67, 68]

Although mesoporous silicas could be considered as useful supports for noble metal nanoparticles due to the expected nanosize confinement effect, the poor affinity between silica and noble metal precursors hinders the optimization of the previously mentioned "collective properties" (nanoparticle size and dispersion) and drastically restricts the catalyst working temperature.[69] In fact, thermal stability constitutes a major drawback to any noble metal based nanomaterials. Hence, when Hüttig and Tamman temperatures are reached, atoms at defects and surfaces and at bulk level will become mobile.[69] Moreover, these temperatures drastically drop down with the particle size.[69] The usual approach to minimize this problem is to modify the host surface with anchoring species able to interact with gold complexes or nanoparticles. For this purpose both organic and inorganic functional groups can be used. As expected, an improved thermal stability is achieved with inorganic anchors like metal oxide nanodomains. In fact noble metal-MO$_x$ materials are good catalysts for a variety of processes.[24, 41, 70] In this work we used NiO$_x$ nanodomains partially embedded inside the silica walls as effective and stable inorganic anchors favoring the nucleation, growth and stability of supported gold particles (see below). In addition to Ni, we included in our supports Ce (or Sn) as oxide domains. Their

incorporation inside the silica walls is supported by different techniques: a) the absence of segregation according to XRD, b) the preservation of the porosity (without significant pore blocking), c) the observation of small black spots (inside the silica-based walls) in the TEM images of Figure 2 that could be attributed to NiOx, SnO$_2$ or CeO$_2$ nanodomains.

A multiple role seems to be played by the CeO$_2$ embedded particles. In a similar way as NiO$_x$, the CeO$_2$ particles could also act as inorganic anchors depending on the specific pH conditions during the impregnation with gold complexes (see above). In fact, ceria is also a typical support for gold nanoparticles.[71] Cerium oxide presents the ability to transport oxygen in combination with the ability to cycle easily between reduced (Ce^{3+}) and oxidized (Ce^{4+}) states.[72] This behavior benefits redox reactions as the benzylamine oxidation. Then, CeO$_2$ could be considered as co-catalyst or promoter. Moreover, the presence in the medium of CeO$_2$ could favor the formation of NiO particles with smaller dimensions avoiding undesired mesopore blocking phenomena.[72] In contrast, no similar benefits are expected in the case of SnO$_2$ included domains. Despite these effects, the presence of nano-oxide domains did not generate an enough strong interfacial interaction with gold nanoparticles to hinder the particle increase with the temperature.

5. Conclusions

The aerobic oxidative condensation of benzylamine to N-benzylidenbenzylamine was carried out on new gold-based catalysts using as supports bimodal UVM-7-like mesoporous silica, containing Ni and Ce (or Sn) as oxide nanodomains partially embedded inside the mesoporous UVM-7 silica walls. These nano-domains acted as effective and stable inorganic anchors favoring the nucleation, growth and stability of supported gold particles. The versatility of the used preparative approach allowed exploiting both the high surface and accessibility of the mesoporous silica and also an easy and homogeneous inclusion of heteroelements in one pot.

Aerobic oxidative condensation of benzylamine on these catalysts occurred selectively only with the formation of N-benzylidenbenzylamine. While the selectivity was total, the conversion varied in a large range as a function of the catalysts composition (chemical composition and atomic ratios of the constitutive support elements). The catalytic behavior was mostly controlled by the size of the gold particles. However, the other heteroelements also have an effect as it is shown in Table 5. Changes in the values of the productivities led also to the conclusion that the support is not a simple spectator for this reaction.

The best results were obtained on gold deposed on the mesoporous Ni$_{10}$-UVM-7(200) as support, ie Au/Ni$_{10}$-UVM-7(200) and Au/Ce$_{60}$-Ni$_{10}$-UVM-7 catalysts. The comparison of the productivities of the individual and bicomponent catalysts led to the conclusion of a cooperative effect between the components. However, the main active specie of these catalysts was gold and the method used for the preparation of these catalysts allowed an enough high dispersion of it to provide the determined activity. The most active catalysts corresponded to the lower Ce content and higher Ni content. TEM and XEDS mapping measurements indicated that the dispersion of these elements ensures the best configurations to activate the deposed Au nano-particles. Smaller Au particle sizes corresponded to the most active catalysts.

None of these catalysts were deactivated by ammonia (that is a by-product of this reaction) and the catalysts were reused for ten times without any evident loss in the activity.

Notes and references

^{a} Department of Organic Chemistry and Catalysis, University of Bucharest, 4-12 Regina Elisabeta Av., 030016 Bucharest, Romania, Tel. +4021410241, E-mail address: vasile.parvulescu@g.unibuc.ro
^{b} Institut de Ciencia dels Material, Universitat de Valencia, P. O. Box 22085, Valencia E46071, Spain, E-mail address: pedro.amoros@uv.es
^{c} Fundació General, Universitat de Valencia, P. O. Box 22085, Valencia E46071, Spain
^{d} Centro de Reconocimiento Molecular y Desarrollo Tecnológico (IDM), Departamento de Química, Universidad Politécnica de Valencia, Camino de Vera s/n, 46022-Valencia, Spain
^{e} National Institute of Materials Physics, PO Box MG-07, 077125 Bucharest-Magurele, Romania

† Electronic Supplementary Information (ESI) available: [details of any supplementary information available should be included here]. See DOI: 10.1039/b000000x/

1. J. R. Wang, Y. Fu, B. B. Zhang, X. Cui, L. Liu and Q. X. Guo, *Tetrahedron Lett.*, 2006, **47**, 8293-8297.
2. J. S. M. Samec, A. H. Ell and J.-E. Backvall, *Chem. Eur. J.*, 2005, **11**, 2327-2334.
3. A. Zanardi, J. A. Mata and E. Peris, *Chem. Eur. J.*, 2010, **16**, 10502-10506.
4. X. Lang, H. Ji, C. Chen, W. Ma and J. Zhao, *Angew. Chem. Int. Ed.*, 2011, **50**, 3934-3937.
5. O. Saidi, A. J. Blacker, M. M. Farah, S. P. Marsden and J. M. J. Williams, *Angew. Chem. Int. Ed.*, 2009, **48**, 7375-7378.
6. Q.-L. Yuan, X.-T. Zhou and H.-B. Ji, *Catal. Commun.*, 2010, **12**, 202-206.
7. A. Grirrane, A. Corma and H. Garcia, *J. Catal.*, 2009, **264**, 138-144.
8. H. Guo, M. Kemell, A. Al-Hunaiti, S. Rautiainen, M. Leskelä and T. Repo, *Catal. Commun.*, 2011, **12** 1260-1264.
9. K. Yamaguchi and N. Mizuno, *Angew. Chem. Int. Ed.*, 2003, **42**, 1480-1483.
10. M. Hosseini-Sarvari, *Chin. Chem. Lett.*, 2011, **22** 547-550.
11. S. M. Landge, V. Atanassova, M. Thimmaiah and B. Torok, *Tetrahedron Lett.*, 2007, **48**, 5161-5164.

12. S. Kamiguchi, A. Nakamura, A. Suzuki, M. Kodomari, M. Nomura, Y. Iwasawa and T. Chihara, *J. Catal.*, 2005, **230**, 204-213.

13. Y. Pérez, C. Aprile, A. Corma and H. Garcia, *Catal. Lett.*, 2010, **134**, 204-209.

14. R. J. Angelici, *Catal. Sci. Technol.*, 2013, **3**, 279-296.

15. L. Aschwanden, T. Mallat, J.-D. Grunwaldt, F. Krumeich and A. Baiker, *J. Mol. Catal. A Chem.*, 2009, **300**, 111-115.

16. K. Rakottyay, A. Kaszonyi and S. Vajıcek, *Appl. Catal. A: General* 2010, **378**, 33-41.

17. B. Zhu, M. Lazar, B. G. Trewyn and R. J. Angelici, *J. Catal.*, 2008, **260**, 1-6.

18. K.-W. Chi, H. Y. Hwang, J. Y. Park and C. W. Lee, *Synth. Metals.*, 2009, **159**, 26-28.

19. K. P. Guzen, A. S. Guarezemini, A. T. G. Orfao, R. Cella, C. M. P. Pereira and H. A. Stefani, *Tetrahedron Lett.*, 2007, **48**, 1845-1848.

20. C. Nicolas, C. Herse and J. Lacour, *Tetrahedron Lett.*, 2005, **46**, 4605-4608.

21. F. Su, S. C. Mathew, S. C. Mohlmann, M. Antonietti, X. Wang and S. Blechert, *Angew. Chem. Int. Ed.*, 2011, **123**, 683.

22. M. T. Schümperli, C. Hammond and I. Hermans, *ACS Catal.*, 2012, **2**, 1108-1117.

23. M. Largeron, *Eur. J. Org. Chem.*, 2013, **2013**, 5225-5235.

24. Y. Zhang, X. Cui, F. Shi and Y. Deng, *Chem. Rev.*, 2012, **112**, 2467-2505.

25. M. Haruta, S. Tsubota, T. Kobayashi, H. Kageyama, M. J. Genet and B. Delmon, *J. Catal.*, 1993, **144**, 175.

26. G. Budroni and A. Corma, *Angew. Chem. Int. Ed.*, 2006, **45**, 3328-3331.

27. R. J. Angelici, *J. Organomet. Chem.*, 2008, **693**, 847-856.

28. A. Grirrane, A. Corma and H. García, *Science*, 2008, **322**, 1661-1664.

29. M.-H. So, Y. Liu, C.-M. Ho and C.-M. Che, *Chem. Asian J.*, 2009, **4**, 1551-1561.

30. L. Aschwanden, T. Mallat, M. Maciejewski, F. Krumeich and A. Baiker, *ChemCatChem*, 2010, **2**, 666-673.

31. L. Al-Hmoud and C. W. Jones, *J. Catal.*, 2013, **301**, 116-124.

32. I. E. Wachs and K. Routray, *ACS Catal.*, 2012, **2**, 1235-1246.

33. A. Villa, G. M. Veith, D. Ferri, A. Weidenkaff, K. A. Perry, S. Campisia and L. Prati, *Catal. Sci. Technol.*, 2013, **3**, 394-399.

34. G. Zhao, H. Hu, W. Chen, Z. Jiang, S. Zhang, J. Huang and Y. Lu, *Catal. Sci. Technol.*, 2013, **3**, 404-408.

35. J. Huang, C. Xue, B. Wang, X. Guo and S. Wang, *Reac. Kinet. Mech. Cat.*, 2013, **108**, 403-416.

36. H. You, R. Liu, C. Liang, S. Yang, F. Wang, X. Lu and B. Ding, *J. Mater. Chem. A*, 2013, **1**, 4097-4104.

37. S. Cabrera, J. El Haskouri, C. Guillem, J. Latorre, A. Beltran, D. Beltran, M. D. Marcos and P. Amoros, *Solid State Sci.*, 2000, **2**, 405-420.

38. J. El Haskouri, D. Ortiz de Zarate, C. Guillem, J. Latorre, M. Caldes, A. Beltran, D. Beltran, A. B. Descalzo, G. Rodriguez, R. Martinez-Mañez, M. D. Marcos and P. Amoros, *Chem. Commun.*, 2002, **4**, 330-331.

39. J. El Haskouri, J. M. Morales, D. Ortiz de Zárate, L. Fernández, J. Latorre, C. Guillem, A. Beltrán, D. Beltrán and P. Amorós, *Inorg. Chem.*, 2008, **47**, 8267-8277.

40. M. Haruta, *Gold Bull.*, 2004, **37**, 27-36.

41. A. Corma and H. García, *Chem. Soc. Rev.*, 2008, **37**, 2096-2126.

42. C. F. Baes and R. E. Mesmer, *In The Hydrolysis of Cations*, John Wiley & Sons, New York 1976.

43. M. Magureanu, N. B. Mandache, J. Hu, R. Richards, M. Florea and V. I. Parvulescu, *Appl. Catal. B: Environmental*, 2007, **76**, 275-281.

44. F. Neatu, Z. Li, R. Richards, P. Y. Toullec, J.-P. Genet, K. Dumbuya, M. J. Gottfried, H. P. Steinrueck, V. I. Parvulescu and V. Michelet, *Chem. Eur. J.*, 2008, **14** 9412-9418.

45. J. El Haskouri, S. Cabrera, C. J. Gómez-García, C. Guillem, J. Latorre, A. Beltrán, D. Beltrán, M. D. Marcos and P. Amorós, *Chem. Mater.*, 2004, **16**, 2805-2813.

46. L. Fernández, N. Garro, J. El Haskouri, M. Pérez-Cabero, J. Alvarez-Rodríguez, J. Latorre, C. Guillem, A. Beltrán, D. Beltrán and P. Amorós, *Nanotechnology*, 2008, **19**, 225603.

47. T. Sakwarathorn, A. Luengnaruemitchai and S. Pongstabodee, *J. Ind. Eng. Chem.*, 2011, **17**, 747-754.

48. P. Zhang, X. Zhou, Y. Tang and T. K. Sham, *Langmuir*, 2005, **21**, 8502-8508.

49. J.-J. Pireaux, M. Liehr, P. Thiry, J.-P. Delrue and R. Caudano, *Surf. Sci.*, 1984, **141**, 221.

50. M. Lenglet, F. Hochu, J. Durr and M. H. Tuilier, *Solid State Commun.*, 1997, **104**, 793-798.

51. P. Prieto, V. Nistor, K. Nouneh, M. Oyama, M. Abd-Lefdil and R. Díaz, *Appl. Surf. Sci.*, 2012, **258**, 8807-8813.

52. M. Chen and X.-M. Zheng, *J. Mol. Catal. A: Chemical*, 2003, **201**, 161-166.

53. V. I. Parvulescu, P. Grange and B. Delmon, *Appl. Catal. B, Environmental*, 2001, **33**, 223-237.

54. L. Liu, S. Zhang, X. Fu and C.-H. Yan, *Chem. Commun.*, 2011, **47**, 10148-10150.

55. X.-F. Wu, A. Petrosyan, T. V. Ghochikyan, A. S. Saghyan and P. Langer, *Tetrahedron Lett.*, 2013, **54**, 3158-3159.

56. V. Parvulescu, S. Coman, L. Frunza, D. Macovei, I. Sandulescu and V. I. Parvulescu, *Stud. Surf. Sci. Catal.*, 1997, **112** 161.

57. C. Tiseanu, V. I. Pârvulescu, M. Boutonnet, B. Cojocaru, P. A. Primus, C. M. Teodorescu, C. Solans and M. S. Dominguez, *Phys. Chem. Chem. Phys.*, 2011, **13**, 17135-17145.

58. M. Lazar and R. J. Angelici, *J. Am. Chem. Soc.*, 2006, **128**, 10613-10620.

59. M. Boronat and A. Corma, *J. Catal.*, 2011, **284**, 138-147.

60. L. Alves, B. Ballesteros, M. Boronat, J. R. Cabrero-Antonino, P. Concepción, A. Corma, M. A. Correa-Duarte and E. Mendoza, *J. Am. Chem. Soc.*, 2011, **133**, 10251-10261.

61. A. Leyva-Pérez, J. Oliver-Meseguer, J. R. Cabrero-Antonino, P. Rubio-Marqués, P. Serna, S. I. Al-Resayes and A. Corma, *ACS Catal.*, 2013, **3**, 1865−1873.

62. C.-R. Chang, X.-F. Yang, B. Long and J. Li, *ACS Catal.*, 2013, **3**, 1693−1699.

63. K. J. Stowers, R. J. Madix and C. M. Friend, *J. Catal.*, 2013, http://dx.doi.org/10.1016/j.jcat.2013.1005.1033.

64. J. L. C. Fajin, M. N. D. S. Cordeiroa and J. R. B. Gomes, *Appl. Catal. A: General*, 2013, **458**, 90-102.

65. V. Atanassova, K. Ganno, A. Kulkarni, S. M. Landge, S. Curtis, M. Foster and B. Török, *Appl. Clay Sci.*, 2011, **53**, 220-226.

66. D. R. Rolison, *Science*, 2003, **299**, 1698-1701.
67. M. Pérez-Cabero, A. B. Hungría, J. M. Morales, M. Tortajada, D. Ramón, A. Moragues, J. El Haskouri, A. Beltrán, D. Beltrán and P. Amorós, *J. Nanopart. Res.*, 2012, **14**, 1045-1057.
68. M. Pérez-Cabero, J. El Haskouri, B. Solsona, I. Vázquez, A. Dejoz, T. García, J. Álvarez-Rodríguez, A. Beltrán, D. Beltrán and P. Amorós, *J. Mater. Chem.*, 2010, **20**, 6780-6788.
69. J. Sun and X. Bao, *Chem. Eur. J.*, 2008, **14**, 7478-7488.
70. G. J. Hutchings, *J. Mater. Chem. A*, 2009, **19**, 1222-1235.
71. S. Carrettin, P. Conception, A. Corma, J. M. Lopez Nieto and V. F. Puntes, *Angew. Chem. Int. Ed.*, 2004, **43**, 2538-2540.
72. B. Solsona, P. Concepción, S. Hernández, B. Demicol and J. M. López-Nieto, *Catal. Today*, 2012, **180**, 51-58.

Catalysis Science & Technology Accepted Manuscript